

Turbulent erosion of a subducting intrusion in the Western Mediterranean Sea

Giovanni Testa¹, Mathieu Dever^{2,3}, Mara Freilich⁴, Amala Mahadevan², T. M. Shaun Johnston⁵, Lorenzo Pasculli^{1,6}, Francesco M. Falcieri¹

¹ Institute of Marine Sciences, Italian National Research Council (CNR-ISMAR), Venice, Italy.

² Woods Hole Oceanographic Institution, Woods Hole, 02543, MA, USA

³ RBR, Ottawa, Canada

⁴ Brown University, Providence, RI, USA

⁵ Scripps Institution of Oceanography, University of California, San Diego, La Jolla, CA, USA

⁶ Department of Environmental Sciences, Informatics and Statistics, University Ca' Foscari of Venice, Via Torino 155, 30172 Mestre, Italy

Correspondence to: Giovanni Testa (giovanni.testa@ve.ismar.cnr.it)

Abstract. Frontal zones within the Western Alboran Gyre (WAG) are characterized by a density gradient resulting from the convergence of Atlantic and Mediterranean waters. Subduction along isopycnals at the WAG periphery can play a crucial role in upper ocean ventilation and influences its stratification and biogeochemical cycles. In 2019, physical parameters (comprising temperature, salinity, turbulent kinetic energy dissipation rates) and biogeochemical data (oxygen and chlorophyll-a) profiles were collected in transects along the northern edge of the WAG. Several intrusions of subducted water with elevated oxygen, chlorophyll-a and spice anomaly were identified towards the center of the anticyclone. These features had elevated kinetic energy dissipation rates on both their upper and lower boundaries. Analysis of the turbulent fluxes involving heat, salt, oxygen, and chlorophyll-a demonstrated a net flux of physical and biogeochemical properties from the intrusions to the surrounding ocean. Either the turbulent or diffusive convection mixing contributed to the observed dilution of the intrusion. Other factors (e.g., water column density stability, variability of the photic layer depth, and organic matter degradation) likely played a role in these dynamics. Enhanced comprehension of the persistence and extent of these features might lead to an improved quantitative parametrization of relevant physical and biogeochemical properties involved in subduction within the study zone.

1 Introduction

The Mediterranean Sea is characterized by a shallow circulation cell and a complex upper-layer circulation featuring numerous quasi-permanent eddies and fronts (Tanhua et al., 2013; Capó et al., 2019; Barral et al., 2021; Bonaduce et al., 2021; Zarokanellos et al., 2022; Sánchez-Garrido and Nadal, 2022). The main 12 Mediterranean thermal fronts were listed by Belkin and Cornillon (2007), whereas a recent work by Sudre et al. (2023) captured an even more complex scenario. Specifically, frontal zones in the Alboran Sea (Western Mediterranean basin) are characterized by a density gradient resulting from the

32 convergence of Atlantic and Mediterranean waters (Fedele et al., 2022; Garcia-Jove et al., 2022). The Atlantic jet strongly
33 influences the formation of two large-scale anticyclonic gyres within the Alboran Sea (the Eastern and Western Alboran Gyres,
34 WAG; **Fig. 1A**) with a smaller cyclonic gyre typically situated in between (Brett et al., 2020; Sala et al., 2022; Sánchez-Garrido
35 and Nadal, 2022).

36 Ocean subduction, defined as the physical transfer of water from the mixed layer into the ocean interior (Williams,
37 2001), plays a pivotal role in upper-ocean ventilation and stratification. It also exerts a profound influence on biogeochemical
38 cycles, thereby contributing to the export of greenhouse gases and the vertical transport of organic carbon (Omand et al., 2015;
39 Olita et al., 2017; Stukel et al., 2017; Ruiz et al., 2019; Zarokanellos et al., 2022). The vertical component of ocean current
40 velocity is typically much smaller than its horizontal counterparts, but areas characterized by meandering frontal features
41 associated with mesoscale eddies are expected to exhibit elevated subduction rates (van Haren et al., 2006). Indeed, vertical
42 velocities of up to 55 m d^{-1} have been observed in the Western Alboran Sea front (Capó and McWilliams, 2022; Garcia-Jove
43 et al., 2022; Rudnick et al., 2022), and net submesoscale subduction rate has been estimated at 0.3 m day^{-1} (Freilich and
44 Mahadevan, 2021). Mesoscale turbulence contains more energy than submesoscale patterns (Storer et al., 2022), although
45 submesoscale features can generate larger vertical velocities than mesoscale structures within frontal zones (Mahadevan, 2016;
46 Ruiz et al., 2019). The relationship between submesoscale velocity and **turbulencemixing** within the boundary layer has been
47 explored in prior studies under conditions of turbulent thermal wind balance (Crowe and Taylor, 2018; McWilliams, 2021)
48 and symmetric instabilities (Thomas et al., 2013; Bachman et al., 2017; Zhou et al., 2022). However, so far there has been
49 limited research that specifically identifies occurrences of quasi-balanced subsurface vertical velocity and examines how
50 **turbulencemixing** responds to such instances.

51 Vertical motion at fronts is driven by frontogenesis, instability processes, nonlinear Ekman effects, and
52 filamentogenesis (Klein and Lapeyre, 2009; Mahadevan, 2016; Mahadevan et al., 2020a; McWilliams, 2021; Capó and
53 McWilliams, 2022; Garcia-Jove et al., 2022). Instabilities have also been identified as a key source of turbulence and energy
54 dissipation at oceanic fronts (D'Asaro et al., 2011; Carpenter et al., 2020; McWilliams, 2021). Subsurface intrusions carry
55 physical (temperature and salinity) and biogeochemical properties (oxygen and chlorophyll-a) characteristic of the surface
56 mixed layer along isopycnals and extend downward and laterally. Intrusions are often identified because of the co-occurrence
57 of subsurface maxima in oxygen, particulate organic carbon with anomalous temperature and salinity properties (i.e., spice;
58 Omand et al., 2015). Intermittent intrusions subducting along the outer periphery of mesoscale and submesoscale structures
59 have previously been identified (Johnston et al., 2011; Llort et al., 2018; Chapman et al., 2020; Johnson and Omand, 2021;
60 Chen et al., 2021; Capó and McWilliams, 2022; Freilich et al., 2024). This study measures the turbulent erosion of a subducting
61 intrusion at fronts within the Western Alboran Gyre ~~(WAG)~~, a major mesoscale feature in the western Mediterranean Sea **with**
62 **a Rossby number of 0.08**. Data were collected in the framework of the Coherent Lagrangian Pathways from the Surface Ocean
63 to Interior (CALYPSO) project onboard the R/V *Pourquois Pas?*, that aimed to examine subduction features in close proximity
64 to the unstable front that developed along the northern edge of the WAG (Mahadevan et al., 2020).

65 Previous studies have investigated turbulence data collected with microstructure probes in both the surface (Cuypers
66 et al., 2012; Forryan et al., 2012; Vladoiu et al., 2021) and deep (Ferron et al., 2021; van Haren, 2023) regions of the Western
67 Mediterranean Sea. However, this work represents the first comprehensive investigation of turbulence in a context of
68 mesoscale-submesoscale subduction at frontal zones within the WAG. This paper begins with a comprehensive description of
69 water column properties and a turbulence dataset. We then conduct an examination of physical and biogeochemical properties
70 across frontal transects to identify and characterize subducting features. Finally, we calculate the turbulent erosion of a selected
71 intrusion of interest.

72 2 Material and methods

73 2.1 Sampling strategy and profile inventory

74 The study zone is highly dynamic and significantly influenced by the eastward-flowing Atlantic jet that sustains the WAG
75 (Sánchez-Garrido and Nadal, 2022). The jet is characterized by a pronounced frontal zone, exhibiting a density contrast of up
76 to 1.0 kg m^{-3} at its boundaries (Oguz et al., 2014).

77 We conducted five transects across the salinity front identified through operational modeling and satellite estimations
78 in the northern edge of the WAG between March 28th and April 4th 2019 (**Fig. 1B**). Temperature and salinity conditions in the
79 upper water column were sampled with an Underway Conductivity Temperature Depth (UCTD) profiler, resulting in a total
80 of 136 profiles (mean depth: 231 m). Turbulence data were collected on 43 stations (mean depth: 219 m) during the campaign-
81 using a microstructure profiler. With the exception of a single station, all stations featured duplicate microstructure profiles,
82 from which the mean value between these replicates was computed. Furthermore, we obtained used a CTD probe to obtain 22
83 dissolved oxygen and chlorophyll-a profiles (mean depth: 284 m) concurrently with the microstructure profiles.

84 2.2. Temperature, salinity and derived variables

85 Temperature and salinity data were acquired using a Teledyne RD Instruments ~~Underway Conductivity Temperature Depth~~
86 ~~(UCTD)~~ profiler, as detailed by Rudnick and Klinke (2007). The sampling rate is 16 Hz, with the UCTD falling velocity
87 ranging between 1.5 and 3.5 m s^{-1} . The spatial resolution between UCTD cycles was approximately 1 km, given a cruise speed
88 of 3 m s^{-1} knots during recovery. The UCTD downcasts were post-processed for sensor alignment, salinity spikes correction
89 and were binned using a spline interpolation onto a vertical grid of 1 m. A comprehensive description of data post-processing
90 procedures can be found in Dever et al., (2019). Key oceanographic parameters, including absolute salinity, conservative
91 temperature, Brunt–Väisälä frequency (N^2), density ratio and Turner angle and spice were computed using the Gibbs Sea
92 Water oceanographic toolbox of TEOS-10 (<https://www.teos-10.org/pubs/gsw>).

93 N^2 serves as an indicator of water column vertical stability and was determined using equation (1):

$$94 \quad N^2 = -\frac{g}{\rho_w} \frac{\partial \rho}{\partial z} \quad (1)$$

95 where g represents gravitational acceleration (9.8 ms^{-2}), ρ_w is a reference seawater density (1025 kg m^{-3}), and $\partial\rho/\partial z$ denotes
 96 the variability of potential density with depth. The density ratio quantifies the vertical contributions of conservative
 97 temperature and absolute salinity to the stability of the water column (following the Thermodynamic Equation of Seawater –
 98 2010; IOC et al., 2010). The Turner angle, as outlined by McDougall et al., (1988), was computed to identify water column
 99 conditions, including double diffusivity (thermal diffusivity or salt fingering), stability, and instability regimes. Seawater spice,
 100 defined as the temperature and salinity variability along isopycnals, was employed to discern water masses with similar density,
 101 but varying temperature and salinity characteristics (McDougall et al., 2021). Spice anomaly was computed with respect to the
 102 mean spice profile computed in a temperature-salinity space ~~and obtained including all spice profiles of the dataset.~~
 103 (McDougall and Krzysik, 2015) and obtained including all spice profiles of the dataset. When computing the mean spice for a
 104 given density, we effectively combine specific temperature and salinity values that correspond to that density. The resulting
 105 spice anomaly then quantifies the deviation of the water parcel with the same density from the mean temperature-salinity
 106 combination, enabling the identification of intrusions. Furthermore, mixed layer depth was determined using a density
 107 threshold of 0.03 kg m^{-3} relative to the reference density at 10 m depth, as proposed by de Boyer Montégut et al. (2004).
 108 Isopycnal strain, which measures the stretching or compression of isopycnal surfaces, was calculated as the vertical gradient
 109 of isopycnal displacement (Pinkel et al., 1991). This displacement is defined as the difference between the actual depth of each
 110 isopycnal and its expected depth based on the mean density profile calculated along the entire section.

111 **2.3. Detection of subducting intrusions**

112 Observational evidence of water being subducted from the upper ocean layer to below the mixed layer was observed by
 113 leveraging the high spatio-temporal resolution of the underway data collected by the UCTD. The presence of subsurface
 114 intrusions in a frontal transect was semi-automatically detected from the vertical profiles, based on subsurface spice and
 115 temperature anomalies. The detection algorithm proceeds as follows: I) Compute average spice on isopycnals for the campaign
 116 (auto). II) Compute spice anomaly on an isopycnal for each profile phase (auto). III) Detect subsurface anomalies in spice
 117 anomaly using a peak-finding algorithm based on peak prominence (auto). IV) Retain anomalies with at least 5 samples (i.e.,
 118 1.5 m; auto) and occur coherently over more than 3 consecutive profiles (manual).

119

120

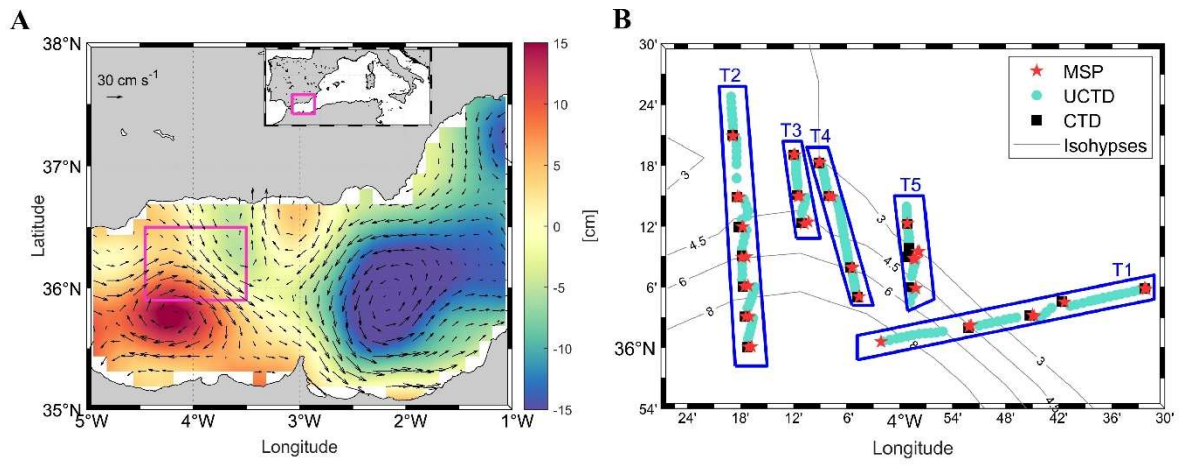


Figure 1. (A) Map of the Alboran Sea showing the mean absolute dynamic topography (colors) and geostrophic currents (arrows) on March 30th-31st, 2019. The purple inset shows the location of the sampling effort, detailed in panel (B), where blue rectangles denote the sampling stations selected for transect (T#) analysis. T1 was realized on March 29th, T2 on March 30th and T3-T5 on March 31st. Isohyps of absolute dynamic topography are depicted as gray lines. Red stars, cyan circles and black squares correspond to sampling stations for the microstructure profiler, underway CTD and CTD, respectively. Daily absolute dynamic topography and geostrophic current data were downloaded from <https://data.marine.copernicus.eu/>.

2.4. Dissolved oxygen and Chlorophyll-a

We equipped a SeaBird 911plus CTD probe with a SeaBird 43 dissolved oxygen sensor and a WET Labs ECO-AFL/FL fluorometer to assess dissolved oxygen and chlorophyll-a concentrations, respectively. The CTD data underwent bin-averaging to achieve a vertical resolution of 0.5 m and was subsequently calibrated using in situ data. Dissolved oxygen estimates were aligned with measurements obtained through Winkler titration ($n = 67$; Mahadevan et al., 2020b), while chlorophyll-a estimates derived from fluorescence were calibrated against data from fluorometric determinations ($n = 140$; Alou-Font et al., 2019). A high level of agreement was found between in situ measurements and CTD-derived estimations, as evidenced by coefficient of determination (R^2) values of 0.99 for dissolved oxygen and 0.85 for chlorophyll-a.

Oxygen and chlorophyll-a anomaly on isopycnals were computed following equation (2):

$$X_a = X_p - \bar{X}_p \quad (2)$$

where X_a represents the variable (i.e., oxygen or chlorophyll-a) anomaly, X_p denotes the observed value at a specific density and \bar{X}_p is the mean property value corresponding to this density.

2.5. Horizontal ocean currents, Richardson number and potential vorticity

Horizontal current magnitude and direction were collected using a hull-mounted Teledyne RDI Ocean Surveyor Acoustic Doppler Current Profiler (ADCP) operating at a frequency of 150 kHz and with a vertical bin size of 4 m. Detailed post-processing procedures for ADCP data have been exhaustively documented in Mahadevan et al. (2020b) and Cutolo et al.

(2022). Shear squared (S^2) was calculated from ADCP data as the sum of the squares of the vertical gradients of the horizontal velocity components (Gregg, 1989). This value was subsequently used to estimate the Richardson number for shear instabilities (expressed as the ratio between N^2 and S^2 ; Cushman-Roisin and Beckers, 2011). Ertel potential vorticity (PV) was calculated according to Zhmur et al. (2021) and equation (3):

$$PV = -(f + \zeta) \frac{\partial b}{\partial z} + \left(\frac{\partial v}{\partial z} \frac{\partial b}{\partial x} - \frac{\partial u}{\partial z} \frac{\partial b}{\partial y} \right) \quad (3)$$

where f is the Coriolis parameter, ζ is the relative vorticity, $\partial b/\partial z$ corresponds to the vertical buoyancy gradient, $\partial b/\partial x$ and $\partial b/\partial y$ are the horizontal buoyancy gradients, and u and v represent the horizontal current components.

2.6. Turbulent kinetic energy dissipation rates

Various methods have been employed to quantify turbulent mixing (e.g., integral approaches, finescale parameterizations and direct microstructure measurements; Thorpe, 2005; Shroyer et al., 2018). In this study, we present turbulence dissipation rates observations and derived parameters (Thorpe, 2005) collected using a free-falling microstructure profiler (MSS90D; Sea & Sun Technology). The probe was equipped with two microstructure shear sensors (PNS6), with the final turbulent dissipation rate calculated as the mean of the two shear probe estimates. The profiler's buoyancy was adjusted to achieve a sinking velocity between 0.6 and 0.7 m s⁻¹ and the data sampling occurred at a frequency of 1024 Hz but was internally averaged to 512 Hz to comply with signal degradation along the 1.2 km probe cable. Post-processing and turbulent dissipation rate calculations were carried out using the microstructure profiler processing toolbox developed by Schultz et al. (2022). We fine-tuned instrument-specific parameters according to the microstructure profiler employed in this study (e.g., sampling frequency, sensors calibration and sensitivity, distance of other sensors to the shear sensor's tip), while the threshold parameters for data validation from Schultz et al. (2022) were retained. These processing routines were evaluated using two benchmark ATOMIX (Analysing Ocean Turbulence Observations to Quantify Mixing) datasets (Fer et al., 2024), which adhere to best practices for estimating dissipation rates from shear probes (Lueck et al., 2024). The analysis showed strong consistency ($R^2 = 0.98$) between ATOMIX data processed using the Schultz et al. (2022) routines and the Lueck et al. (2024) approach (Supplementary Fig. 1), with the former slightly overestimating dissipation rates by a mean of 1.6%.

Kinetic energy dissipation rates (ϵ) were computed as per equation (34):

$$\epsilon = 15\nu \overline{\left(\frac{\partial u}{\partial z}\right)^2} \quad (34)$$

where ν represents the kinematic molecular viscosity and $\overline{(\partial u/\partial z)^2}$ is the spatial average of vertical shear variation with depth (Taylor, 1935). Turbulent dissipation rates from both shear probes were treated separately, averaging all shear spectra within 1 m vertical bin. The shear spectrum results were iteratively fitted to the Nasmyth (Nasmyth, 1970) reference shear spectrum and the deviation of the observed spectrum with respect to the Nasmyth's was used for data quality check. A detailed description of the data processing procedure was described in Schultz et al. (2022). We performed data-averaging at 1-meter

175 depth intervals, excluding the initial 15 meters of each profile, to mitigate the noise arising from ship motion and wave-
176 breaking (D'Asaro, 2014).

177 The microstructure data exhibited good agreement ($R^2 = 0.89$) between the two shear sensors ($n=8957$;
178 **Supplementary Fig. 1A2A**), with a stronger correlation observed under elevated turbulence conditions ($\epsilon > 10^{-7} \text{ W kg}^{-1}$)
179 compared to calmer waters ($\epsilon < 10^{-7} \text{ W kg}^{-1}$). Another quality control parameter was the magnitude of the pseudo dissipation
180 rates originated from the profiler high frequency vibrations, consistently one order of magnitude lower than turbulent kinetic
181 energy dissipation rates (**Supplementary Fig. 1B2B**) and predominantly (36.9%) falling within the range of $1.0 \cdot 10^{-10}$ to $1.6 \cdot 10^{-10}$
182 W kg^{-1} .

183 2.7 Turbulent fluxes

184 Vertical diffusivity (K_z) is computed according to equation (45):

$$185 K_z = \gamma \frac{\epsilon}{N^2} \quad (45)$$

186 where the mixing efficiency is $\gamma = 0.2$ (Gregg et al., 2018; Mouriño-Carballido et al., 2021; Lozovatsky et al., 2022), ϵ is the
187 turbulent kinetic energy dissipation rate and N^2 denotes the squared buoyancy frequency.

188 We determine turbulent heat (in units of W m^{-2}) and salt fluxes ($\text{kg m}^{-2} \text{s}^{-1}$) following Sheehan et al. (2023) and
189 equations (56) and (67):

$$190 Q_H = -\rho C_p K_z \frac{\partial \theta}{\partial z} \quad (56)$$

$$191 Q_S = 10^{-3} \left(-\rho K_z \frac{\partial S}{\partial z} \right) \quad (67)$$

192 where ρ is seawater density, C_p is the specific heat capacity of seawater ($3850 \text{ J kg}^{-1} \text{ }^\circ\text{C}^{-1}$), $\partial\theta/\partial z$ corresponds to the vertical
193 gradient of conservative temperature, and $\partial S/\partial z$ indicates the vertical gradient of absolute salinity. Furthermore, turbulent
194 fluxes of dissolved oxygen and chlorophyll-a (in units of $\text{mg m}^{-2} \text{s}^{-1}$) were estimated using equations (78) proposed by Williams
195 et al. (2013):

$$196 Q_X = -K_z \frac{\partial X}{\partial z} \quad (78)$$

197 where ∂X denote the variable (i.e., oxygen or chlorophyll-a) vertical gradient with depth.

198 Our analysis primarily focused on the subducting intrusion identified along transect 2 during the 2019 CALYPSO campaign
199 (**Fig. 1B**). The limited number of microstructure profiles precluded a comprehensive analysis of spatiotemporal intrusions
200 variability along the other transects. To assess the physical and biogeochemical conditions around the subducting intrusion
201 boundaries, we calculated the mean conditions within 5 m inside and outside the intrusion boundaries. The methodology used
202 to calculate diapycnal turbulent fluxes does not account for advective terms involving diapycnal velocity (Du et al., 2017) and
203 assume a constant mixing efficiency (γ) of 0.2. However, γ can vary depending on stratification, turbulence intensity, and water
204 column regimes (Canuto et al., 2011; Gregg et al., 2018). Despite this, variability in γ is typically smaller compared to

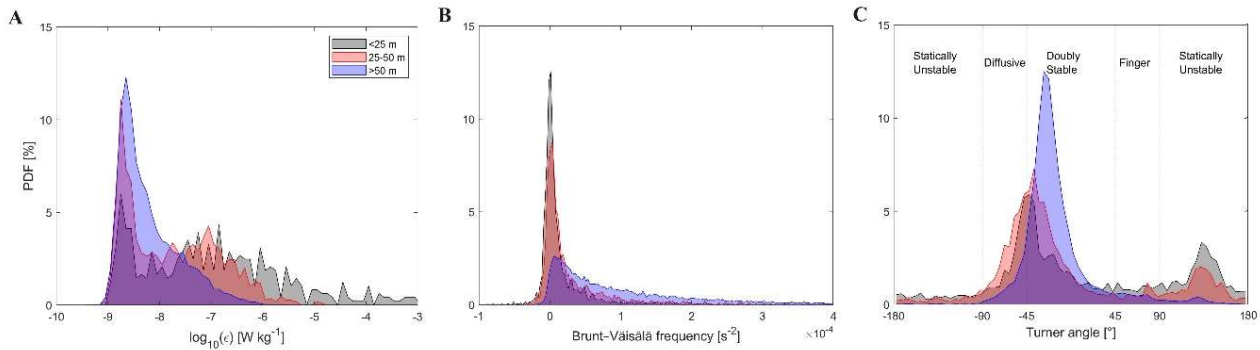
205 variations in turbulence (Le Boyer et al., 2023). It is important to note that the assumption of identical vertical diffusivity for
 206 heat, salt, and tracers may introduce potential inaccuracies in flux estimates, which should be considered.

207 3 Results

208 3.1 Water column stability and turbulent kinetic energy dissipation rates

209 High mixing was observed in the surface layer, with localized turbulence peaks in the subsurface water column. Turbulent
 210 kinetic energy (TKE) dissipation values displayed considerable variability, with 43.8% of observations falling between $1.3 \cdot 10^{-9}$
 211 9 and $4.0 \cdot 10^{-9} \text{ W kg}^{-1}$ (mean \pm standard deviation: $8.2 \cdot 10^{-9} \pm 2.4 \cdot 10^{-8} \text{ W kg}^{-1}$), with a peak (11.2%) identified in the range of
 212 $2.0 \cdot 10^{-9}$ to $2.5 \cdot 10^{-9} \text{ W kg}^{-1}$. An analysis of ϵ probability distribution by depth intervals indicated that 95% of deep ϵ values were
 213 comprised between 10^{-9} and $10^{-7} \text{ W kg}^{-1}$ (**Fig. 2A**). In contrast, surface and mid-water depths exhibited a lower proportion
 214 (53% and 77%, respectively) within this ϵ range. Surface waters (<25 m) were characterized by elevated ϵ values, with 25%
 215 and 12% of the data falling within the ranges of 10^{-7} - 10^{-6} and 10^{-6} - $10^{-5} \text{ W kg}^{-1}$, respectively.

216 Elevated homogeneity in the shallow water column vertical structure was observed. Indeed, the probability
 217 distribution of Brunt–Väisälä frequency (N^2) by depth intervals (**Fig. 2B**) indicated lower stratification in the surface and mid-
 218 water layers, where approximately 81% and 67% of values were lower than $0.2 \cdot 10^{-4} \text{ s}^{-2}$, respectively. Conversely, the deeper
 219 portion (>50 m) of the water column exhibited stronger stratification, with an increased proportion (70%) of N^2 estimations
 220 exceeding $0.3 \cdot 10^{-4} \text{ s}^{-2}$. These patterns were reflected in water column regimes conditions. Examination of Turner angle values
 221 revealed a predominantly stable water column, accounting for 74% of the dataset (**Fig. 2C**). However, these stability conditions
 222 exhibited notable variations with depth. The shallow layer displayed a more varied scenario with a near-equal distribution
 223 between statically unstable and doubly stable conditions. In contrast, the mid-water column featured the highest proportion
 224 (27%) of diffusive regimes and the deep layer was primarily characterized (83%) by double stable conditions.



225
 226 **Figure 2.** Probability distribution frequency (PDF) by depth intervals for turbulent kinetic energy dissipation rates (A), Brunt–Väisälä
 227 frequency (B) and Turner angle values (C). Colored shaded areas in panels correspond to different depth intervals, with gray: 15-25 m; red:
 228 26-50 m; blue: depths >51 m. The names in panel (C) reflect the water column regime according to the Turner angle value (McDougall et
 229 al., 1988).

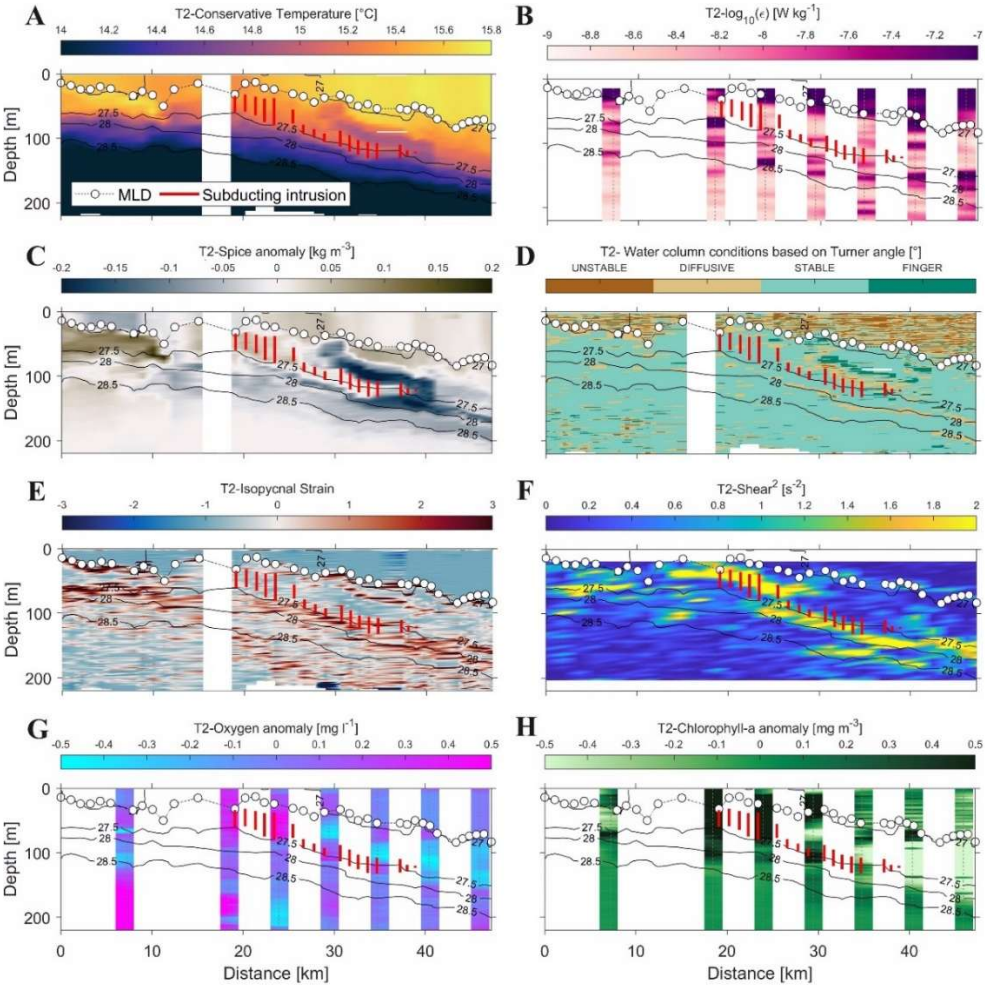
231 3.2 Transects across the Western Alboran Gyre front

232 A noticeable depression in the isopycnals was consistently observed in all the transects extending towards the interior of the
 233 anticyclone (**Fig. 3** and **Supplementary Fig. 2-63-7**). The highest ϵ below the mixed layer was detected adjacent to zones
 234 featuring elevated vertical density gradients and deepening along the isopycnals in transects 2 (**Fig. 3**). A deepening of positive
 235 spice anomalies from approximately 50 to 100 m was observed at the start of transect 1 and from 15-35 km of transect 2.
 236 Subducting intrusions were observed along all transects, except for transect 3, possibly owing to its shorter length
 237 (approximately 12 km; **Fig. 3** and **Supplementary Fig. 2-63-7**). The mean thickness of subducting intrusions was computed
 238 at 14.2 m (standard deviation: 9.4 m), ranging from a minimum of 1.7 to a maximum of 42.2 m. The subduction is likely
 239 occurring along the frontal direction, following the anticyclonic circulation, rather than necessarily along the tilted isopycnals
 240 identified in the transect.

241 ~~The subduction is likely occurring along the front and not necessarily along the tilted isopycnal.~~ Enhanced ϵ and
 242 diffusivity values were noted in proximity to the base of the mixed layer and in the vicinity of subducting intrusion boundaries
 243 (**Fig. 4**). Furthermore, diffusive water column conditions were identified along the upper boundary of the subducting intrusion
 244 in transect 2 (**Fig. 3D**) and adjacent to the subducting intrusions within transects 1 and 4. Positive isopycnal strain values were
 245 observed at both edges of the subducting intrusion initially, with a predominant concentration of positive values indicating
 246 stretching of isopycnal surfaces primarily at the bottom edge as subduction progressed. ~~(**Fig. 3E**).~~ The current data along
 247 transect 2 illustrated a horizontal velocity magnitude exceeding 60 cm s^{-1} within the interior of the anticyclone, while lower
 248 values were observed on its periphery. The subducting intrusion, identified beneath the superficial high-velocity patch and
 249 within a zone of elevated shear squared (primarily due to a negative vertical gradient of the zonal velocity component; **Fig. 3**),
 250 ~~was characterized by a horizontal velocity estimated at approximately 0.5 m s^{-1} .~~ **3F**, was characterized by a horizontal velocity
 251 estimated at approximately 0.5 m s^{-1} . The mean Richardson number across the transect was calculated to be 0.89, indicating a
 252 generally stable water column with respect to shear instabilities. However, lower Richardson numbers were observed in the
 253 initial zone of the intrusion (between km 17 and 29 of the transect; **Fig. 3G**). No significant correlation was found between
 254 shear and ϵ , suggesting that stratification may suppress shear-driven turbulence and/or that other sources of turbulence could
 255 be influencing the study area. The subducted water exhibited positive potential vorticity (**Fig. 3H**), revealing unfavourable
 256 conditions for the generation of symmetric instability.

257 A deepening of the well oxygenated surface layer towards the center of the anticyclone was observed in transects 1
 258 and 2 (**Supplementary Fig. 23** and **Fig. 3**, respectively). Elevated dissolved oxygen anomaly concentrations ($>0.5 \text{ mg l}^{-1}$)
 259 were detected inside the subducting intrusion along transect 2 (**Fig. 33I**), with high values deepening from approximately 50
 260 to 120 m. Similarly, anomalous high chlorophyll-a anomaly values were found near the 30 km of transect 2, with anomaly
 261 concentrations of up to 1.4 mg m^{-3} detected at a depth of 100 m. **(Fig. 3J).**

262



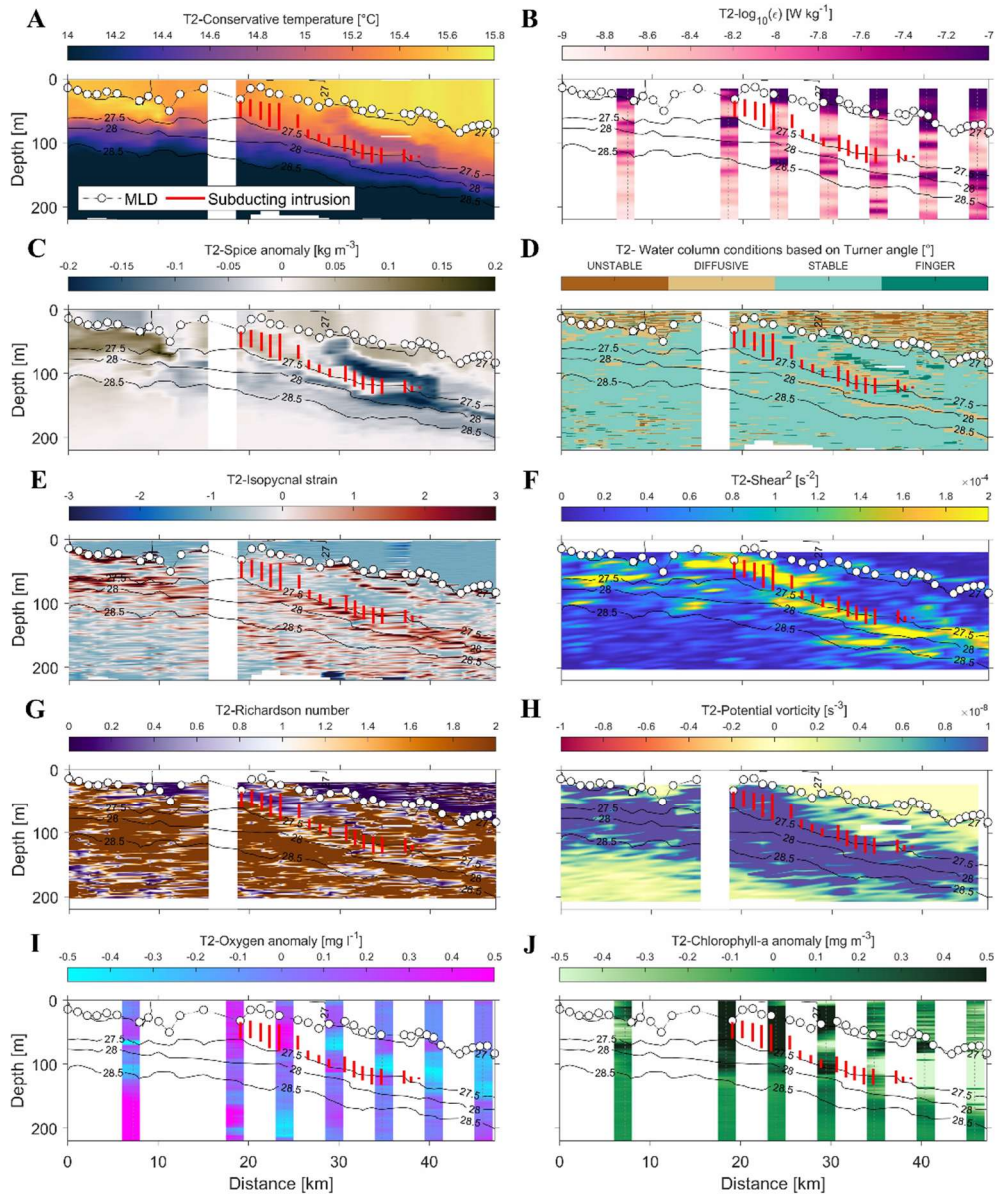


Figure 3. Profiles of conservative temperature (A), turbulent kinetic energy dissipation rates (B), spice anomaly (C), water column conditions based on Turner angle estimations (D), isopycnal strain (E), shear squared (F), Richardson number (G), potential vorticity (H), dissolved oxygen anomaly (I), and chlorophyll-a anomaly (J) estimations acquired along transect 2 of the 2019 CALYSPSO campaign. Isopycnals are represented as black lines, while the mixed layer depth and subducting intrusions are denoted by colored points and lines, respectively. The distances between stations were calculated starting from the northernmost sampling point.

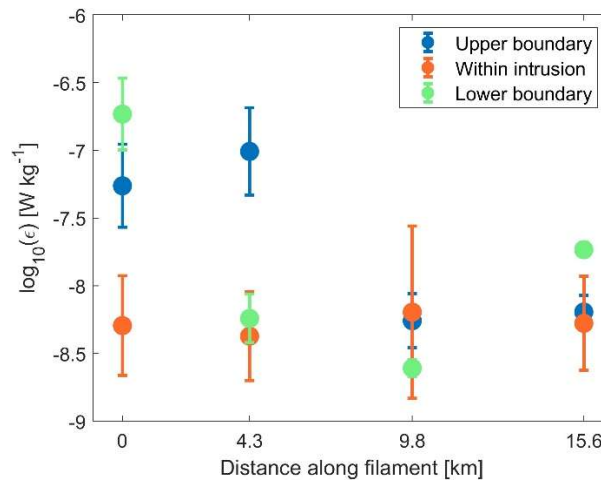


Figure 4. Mean turbulent kinetic energy dissipation values within the intrusion and at its upper and lower boundaries (5 m from the intrusion edges). The errorbars represent the measurement standard deviation.

3.3 Turbulent fluxes around the subducting intrusion

We focused our analysis of the microstructure profiles to transect 2 during the 2019 CALYPSO campaign due to its higher horizontal resolution (**Fig. 1B**). Turbulent fluxes within the interior of the transect 2 intrusion exhibited reduced values compared to water column around both intrusion edges (**Supplementary Fig. 78**). Notably, turbulent fluxes exhibited higher magnitudes within the first two profiles sampling the edges of the subducting intrusion in comparison to the subsequent two profiles (**Fig. 5**). Turbulent fluxes around the intrusion boundaries resulted in a net loss of heat, oxygen and chlorophyll-a properties from within the intrusion to the surrounding ocean, while salinity increased (**Table 1**). Heat, oxygen and chlorophyll-a turbulent fluxes exhibited negative values (i.e., indicating downward direction) revealed a consistent properties loss at the base of the intrusion towards the deeper layer, while salt fluxes displayed positive values (i.e., upward direction) a coherent property loss (gain) at both boundaries the upper (lower) boundary of the intrusion. Positive heat flux values were Heat loss was consistently recorded near the upper intrusion boundary at all sampling stations, although more variability was observed in oxygen and chlorophyll-a fluxes. The mean absolute values for turbulent fluxes indicated reduced heat, oxygen and chlorophyll-a fluxes near the upper boundary in contrast to the intrusion's base. Specifically, the upper heat flux accounted for only 35% of the magnitude observed near the base of the intrusion, while the upper oxygen and chlorophyll-a fluxes represented 68 and 63%, respectively, of the corresponding bottom flux magnitudes. The fluxes uncertainty was provided in **Supplementary Table 1**.

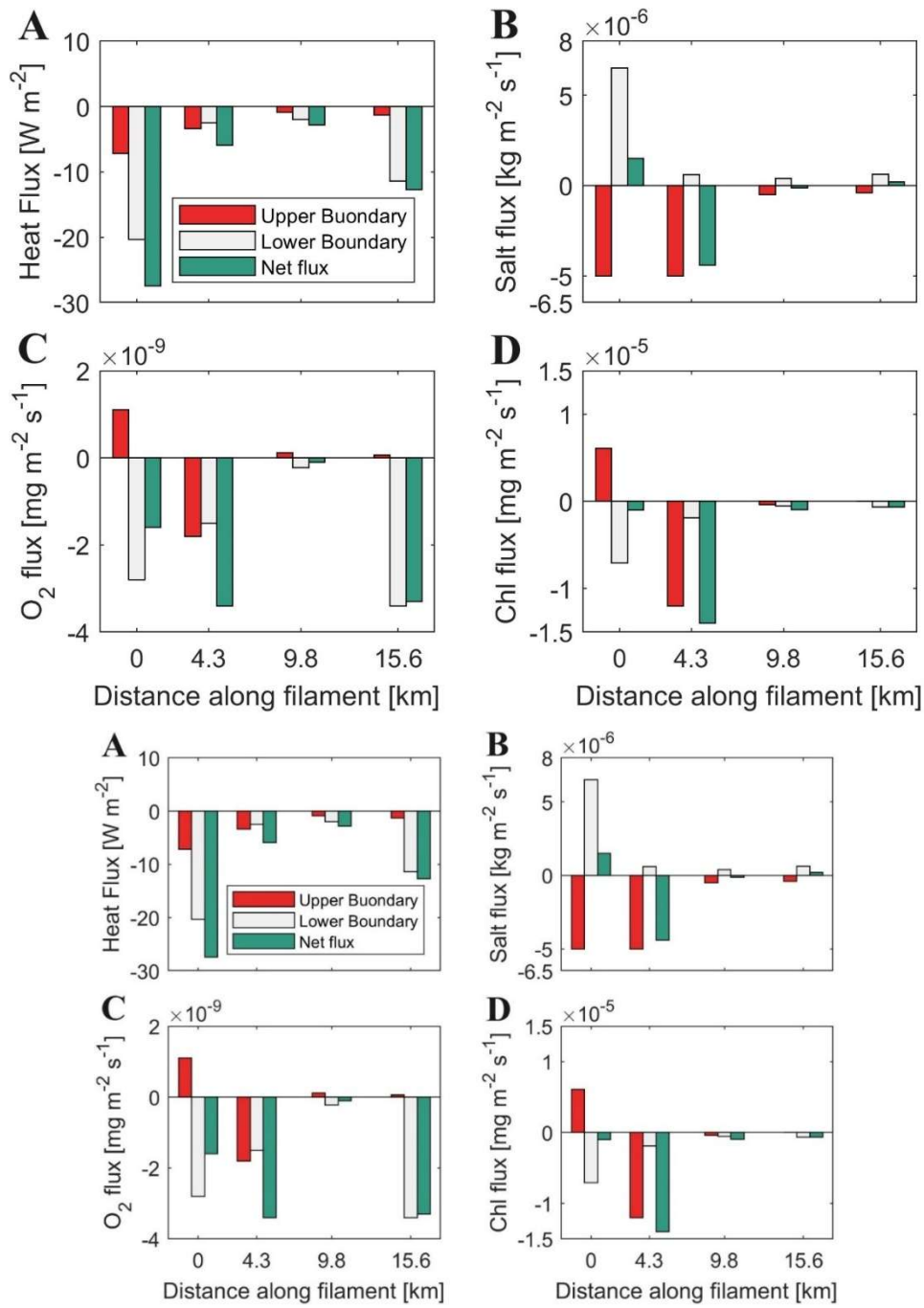


Figure 5. Estimations of turbulent fluxes of heat (A), salt (B), oxygen (C) and chlorophyll-a (D) along the upper and lower boundaries of the subducting intrusion identified within transect T2 of the 2019 CALYPSO campaign and the resulting net flux (in green). The distances between the four stations where the fluxes were calculated (as shown in Supplementary Figure 78) along the subducting intrusion are provided. Positive (negative) values for the turbulent fluxes represent a gain (loss) of the respective variables within the interior of the intrusion.

301 **Table 1.** Mean (\pm 95% confidence interval) conservative temperature, absolute salinity, dissolved oxygen and chlorophyll-a conditions
 302 within the subducting intrusion identified along transect T2- and estimations of daily turbulent heat, salt, oxygen and chlorophyll-a fluxes.
 303 The fluxes were computed as the rate of change of properties $[(\Delta \text{flux}) (\text{intrusion width})^{-1}]$. Negative (positive) values denote a loss (gain)
 304 within the interior of the intrusion. The distances between the four stations, the intrusion mean depth and thickness are provided.

Variable	Distance <u>along transect [km]</u>			
	<u>0</u>	<u>4.3</u>	<u>9.8</u>	<u>15.6</u>
<u>Intrusion characteristics</u>				
<u>Depth [m]</u>	<u>47</u>	<u>59</u>	<u>99</u>	<u>120</u>
<u>Thickness [m]</u>	<u>25.9</u>	<u>42.2</u>	<u>13.3</u>	24.9
<u>Mean properties</u>				
<u>Temperature [°C]</u>	47 15.28 \pm 0.05	59 <u>15.27 \pm 0.06</u>	99 <u>15.16 \pm 0.03</u>	120 <u>14.91 \pm 0.07</u>
<u>Salinity [g kg⁻¹]</u>	4.3 <u>37.03 \pm 0.06</u>	59 <u>37.04 \pm 0.04</u>	9.8 <u>37.10 \pm 0.10</u>	15.6 <u>37.15 \pm 0.28</u>
<u>Oxygen [mg l⁻¹]</u>	99 <u>167.74 \pm 0.03</u>	59 <u>167.84 \pm 0.03</u>	99 <u>7.43 \pm 0.05</u>	120 <u>1387.16 \pm 0.13</u>
<u>Chlorophyll-a [mg m⁻³]</u>	120 <u>14.91 \pm 0.06</u>	59 <u>152.16 \pm 0.07</u>	9.8 <u>161.38 \pm 0.04</u>	15.6 <u>0.68 \pm 0.02</u>
<u>Daily fluxes</u>				
<u>Heat [°C d⁻¹]</u>	<u>-2.2 $\cdot 10^{-2}$</u>	<u>-2.9 $\cdot 10^{-3}$</u>	<u>-4.4 $\cdot 10^{-3}$</u>	<u>-1.1 $\cdot 10^{-2}$</u>
<u>Salt [g kg⁻¹ d⁻¹]</u>	<u>5.1 $\cdot 10^{-3}$</u>	<u>-9.1 $\cdot 10^{-3}$</u>	<u>-7.6 $\cdot 10^{-4}$</u>	<u>7.0 $\cdot 10^{-4}$</u>
<u>Oxygen [mg l⁻¹ d⁻¹]</u>	<u>-5.5 $\cdot 10^{-3}$</u>	<u>-6.9 $\cdot 10^{-3}$</u>	<u>-6.7 $\cdot 10^{-4}$</u>	<u>-1.1 $\cdot 10^{-2}$</u>
<u>Chlorophyll-a [mg m⁻³ d⁻¹]</u>	<u>-3.4 $\cdot 10^{-3}$</u>	<u>-2.9 $\cdot 10^{-2}$</u>	<u>-6.2 $\cdot 10^{-3}$</u>	<u>-2.2 $\cdot 10^{-3}$</u>

307 4 Discussion

308 4.1 Turbulent kinetic energy dissipation rates in the Western Alboran Sea

309 The TKE dissipation rates in our study were (mean: $8.2 \cdot 10^{-9}$ W kg⁻¹) found to be comparable to those reported in previous
 310 investigations involving microstructure data in the Mediterranean Sea. For instance, Cuypers et al. (2012) calculated mean
 311 TKE dissipation values of approximately 10^{-8} W kg⁻¹ below the seasonal pycnocline. Our TKE dissipation estimates unveiled
 312 an intermediate turbulent environment, between the Mediterranean energetic and quiescent regions (mean: $5.2 \cdot 10^{-8}$ and $4.7 \cdot 10^{-8}$
 313 10 W kg⁻¹, respectively; Vladoiu et al., 2021). Interestingly, our findings exhibited a closer resemblance to the TKE dissipation
 314 observed west of the Gibraltar Strait, where the mean TKE dissipation was $4 \cdot 10^{-9}$ W kg⁻¹ in the ocean interior (Fernández-
 315 Castro et al., 2014).

316 The observed peaks in TKE dissipation rates were predictably situated in shallow ocean regions influenced by wave
 317 breaking, in close proximity to the base of mixed layer (Zippel et al., 2022) and near the boundaries of subducting intrusions

(Fig. 3). However, other peaks were detected at deeper levels and did not appear to correlate with aforementioned factors. Mixing processes in the stratified ocean below the mixed layer are often attributed to vertical shear extending below the MLD, penetrative convection and the breaking of internal waves (MacKinnon et al., 2013). The Western Alboran Sea may be influenced by the eastward propagation of internal waves traveling along isopycnals generated by the interaction of tidal currents with bathymetry at the Gibraltar Strait (Thorpe, 2007; Alpers et al., 2008; Bolado-Penagos et al., 2023). While symmetric instabilities have been identified as effective mechanisms for geostrophic energy dissipation in the ocean interior (Zhou et al., 2022), the positive sign of the potential vorticity associated with subducting water in the study area (Freilich and Mahadevan, 2021 Fig. 3H) suggests that the conditions required for this process to occur may not be met. Another plausible explanation for the deep TKE dissipation peaks could be provided by dissipation associated with subducting intrusions that may have gone undetected by our methodology. Conducting future surveys with mooring and/or glider deployments to identify internal waves within the study zone could significantly advance our comprehension of their spatiotemporal variability and their role in generating deep turbulence along isopycnals.

4.2 Water column regimes

The convergence of Atlantic and Mediterranean waters in the study zone resulted in a robust stratification of the water column, characterized predominantly by doubly stable conditions. Along isopycnals and at the upper boundary of the subducting intrusion (Figure 3), we observed instances of diffusive convection regimes. While diffusive convection is typically associated with thermohaline staircases and is more commonly found at higher latitudes (Kelley et al., 2002; van der Boog et al., 2021), the presence of horizontal variability in temperature and salinity conditions in our study area may lead to the formation of coherent subducting intrusions associated with double diffusive convection (Kelley et al., 2002; Schmitt, 2009). Freilich and Mahadevan (2021) proposed that the specific pathway of subducting intrusions along isopycnals in the study zone could be generated by a combination of mesoscale (geostrophic) frontogenesis and submesoscale (ageostrophic) dynamics.

The subducting intrusion transports subsurface water column properties into the deeper ocean, undergoing erosion along its pathway through a combination of turbulent and diffusive mixing. This dynamic process results in a modification of its inherent properties.

4.3 Turbulent erosion of the intrusion

The elevated TKE diffusivitydissipation rates in the surface layer, coupled with an increase in stratification with depth can potentially account for the higher diffusivity and turbulent fluxes observed at the start of the intrusion's subduction compared to stations sampled further along the subduction path. Moreover, physical and biogeochemical properties of the subducted water resembled surface conditions more closely than those of the deep layer, resulting in reduced fluxes along the upper boundary of the intrusion compared to the lower boundary (with the exception of the station located at 4.3 km).

The turbulent erosion of the subducting filament led to an overall decrease in temperature, oxygen and chlorophyll-a content within the filament, while salinity increased (Table 1). The slight increment in oxygen and chlorophyll-a concentration

observed at the second station within the intrusion may be attributed to either ~~downward fluxes~~ the properties gain detected at the upper boundary of the first station, indicating a supply of biogeochemical properties from the surface layer into the intrusion interior, or in situ phytoplankton production (the photic layer was estimated to be around 60 m deep; **Supplementary Fig. 89**).

However, these diapycnal fluxes were too weak to induce a significant dilution of the intrusion, as daily fluxes (~~Supplementary Table 2~~) were orders of magnitude smaller than the mean property values within the intrusion. ~~(Table 1)~~. These estimates did not account for double-diffusive mixing fluxes characteristic of thermohaline staircases, as such features are predominant at greater depths in the Western Mediterranean Sea (Onken and Brambilla, 2003; Schroeder et al., 2016; Ferron et al., 2021). ~~Along the upper boundary of the intrusion, diffusive convection regimes were identified, resulting from the subduction of warmer and less saline water by the intrusion.~~ Despite of this, ~~an estimate~~ the estimates of diffusive convection mixing ~~indicated that these fluxes were generally an order of magnitude lower than were negligible compared to the~~ turbulent fluxes, ~~suggesting a limited impact on intrusion dilution or enrichment (Supplementary Table 2).~~

~~.~~ In addition to turbulent and diffusive convection mixing, ~~various factors~~ the water column density stability and isopycnal mixing might contribute to the typical vertical variability in subsurface ocean temperature and salinity. ~~These factors include the attenuation of solar irradiation, the evaporation-precipitation budget, water column density stability and isopycnal mixing.~~ Specifically, isopycnal mixing might act an important role in the observed dilution given its contribution in meso- and submesoscale coherent features (Abernathey et al., 2022). Conversely, the decline in oxygen and chlorophyll-a content with depth can be attributed to the deepening of the photic layer, distance from the atmospheric-ocean boundary layer, and processes such as remineralization, respiration, and grazing. The modification of the typical vertical variability in biogeochemical properties induced by subducting intrusions might have profound impacts on ecosystem dynamics within the study zone.

4.4 Biogeochemical significance of subducting intrusions

The Atlantic Jet, which enters the Mediterranean through the Strait of Gibraltar, coupled with coastal upwelling events, transforms our study area into one of the most productive zones in the Mediterranean despite the Mediterranean Sea's well-known status as an oligotrophic basin (Reale et al., 2020; Sánchez-Garrido and Nadal, 2022). The outer boundary of the WAG has also been identified as a stirring region where properties of the water column are continually exchanged as they are advected towards the center of the anticyclone (Brett et al., 2020; Sala et al., 2022). Subduction of the intrusion may enhance particulate organic carbon export below the mixed layer, reducing its exposure time to remineralization (Freilich et al., 2024). This process contributes to one of the highest export rates observed in the Mediterranean Sea based on sediment trap and particle size distribution profiles data (Ramondenc et al., 2016). Additionally, the mixing associated with subducting intrusions may facilitate the reorganization of phytoplankton communities, traditionally stratified in the photic layer (Mena et al., 2019) and their proliferation. This is especially significant, as nitrates are nearly depleted in the shallow layer north of the WAG (Oguz et al., 2014; Lazzari et al., 2016; García-Martínez et al., 2018). It has been demonstrated that oceanic fronts might act as aggregation areas for planktonic organisms, becoming important foraging areas for higher trophic layers (Acha et al., 2015). Moreover, the transport of chlorophyll-a towards the center of the WAG could lead to an increase in the biomass of diel vertical

383 migrant zooplankton, which tends to be more abundant in the inner part of the gyre compared to its periphery (Yebra et al.,
384 2018).

385 **5 Conclusions**

386 The Western Alboran Gyre is a dynamical feature characterized by high spatiotemporal variability arising from the
387 convergence of Mediterranean and Atlantic waters. Indeed, the northern edge of the WAG water column exhibited notable
388 spatial variability in both physical and biogeochemical characteristics. Specifically, the inner part of this gyre featured higher
389 temperature, current velocity, oxygen content and chlorophyll-a concentration compared to its periphery. Moreover, there was
390 an observable deepening of enhanced Brunt–Väisälä frequency and turbulent kinetic energy dissipation rates towards the
391 anticyclone’s center.

392 The investigation of spice anomaly spatial variability allowed the identification of several subducting intrusions
393 occurring beneath the mixed layer depth, extending from the gyre’s outer region towards its center. High turbulent kinetic
394 energy dissipation rates were evident at both the upper and lower boundaries of these intrusions, complemented by localized
395 peaks at deeper levels. The specific factors contributing to these heightened dissipation rates at deeper levels remain elusive.

396 The turbulent fluxes of heat, salt, oxygen and chlorophyll-a along the intrusion boundaries revealed a consistent net
397 loss of physical and biogeochemical properties from within the intrusion to the surrounding ocean. From a biogeochemical
398 perspective, the subduction intrusion holds significance as it has the potential to amplify the export of particulate organic
399 carbon below the mixed layer. Additionally, it may contribute to the enhancement of diel vertical migrant zooplankton biomass
400 and facilitate the proliferation of phytoplankton communities. Notably, mixing due to turbulence or diffusive convection
401 contributed little to the observed variation in temperature, salinity, oxygen or chlorophyll-a within the intrusion interior. Other
402 factors, such as water column density stability, variability of the photic layer depth, and organic matter degradation, likely
403 played a role in these dynamics.

404 While our present study has provided valuable insights into the subduction of intrusions and their turbulent erosion
405 within the Western Alboran Gyre, significant gaps remain in our understanding of the spatiotemporal variability of subducting
406 intrusions. Future targeted surveys that specifically address the persistence and extent of these features might improve
407 quantitative parametrizations of key physical and biogeochemical property subduction. Explorations encompassing a broader
408 surface of the WAG may reveal asymmetries in intrusion subduction between the WAG’s edges and offer an estimate of the
409 total subduction occurring within the WAG.

410

411 *Funding.* CALYPSO constitutes a Departmental Research Initiative funded by the U.S. Office of Naval Research. GT was
412 founded by ISMAR-26-2022-VE [and ISMAR-18-2023-VE](#) research [fellowshipfellowships](#). TMSJ was supported by ONR
413 grant N00014-18-1-2416.

414

415 *Data availability.* Data will be made available on request.

416
417 *Author contributions.* GT: Conceptualization, Methodology, Software, Validation, Formal analysis, Data Curation, Writing -
418 Original Draft, Writing - Review & Editing, Visualization. MD: Methodology, Software, Data Curation, Writing - Original
419 Draft, Writing - Review & Editing, Supervision. MF: Resources, Writing - Review & Editing. AM: Resources, Writing -
420 Review & Editing, Project administration, Funding acquisition. SJ: Resources, Writing - Review & Editing. LP: Resources,
421 Writing - Review & Editing. FF: Conceptualization, Methodology, Software, Data Curation, Writing - Original Draft, Writing
422 - Review & Editing, Supervision, Project administration, Funding acquisition.

423
424 *Competing interests.* The authors declare that they have no conflict of interest.

425
426 *Acknowledgements.* We extend our sincere appreciation to the captains and crews of the R/V *Pourquoi Pas?*, as well as the
427 technical and scientific personnel involved in making measurements and providing support. The authors wish to express their
428 gratitude to Leo Middleton engaging in insightful conversations that influenced the development of this article. Furthermore,
429 we would like to acknowledge all the CALYPSO researchers whose constructive comments during CALYPSO's Padua
430 meeting enriched this study. Finally, we thank the editor and reviewers for their valuable assistance, comments, and
431 suggestions.

433 **References**

- 434 Abernathy, R., Gnanadesikan, A., Pradal, M. A., and Sundermeyer, M. A.: Isopycnal mixing, in: Ocean Mixing: Drivers,
435 Mechanisms and Impacts, edited by: Meredith, M., and Naveira Garabato, A., Elsevier, 215–256,
436 <https://doi.org/10.1016/B978-0-12-821512-8.00016-5>, 2022.
- 437 Acha, E. M., Piola, A., Iribarne, O., and Mianzan, H (Eds.): Ecological processes at marine fronts: Oases in the ocean,
438 Springer, Berlin, Germany, 68 pp., ISBN 978-3-319-15479-4, 2015.
- 439 Alou-Font, M., Carbonero, A., and Allen, J.: NRV Alliance report on delayed mode calibration of chlorophyll data.
440 CALYPSO19 cruise 28-03/10-04/19 V-1.0.0, SOCIB-Biogeochemistry Tech. Rep., 2019.
- 441 Alpers, W., Brandt, P., and Rubino, A.: Internal waves generated in the Straits of Gibraltar and Messina: Observations from
442 space, in: Remote Sensing of the European Seas, Springer Netherlands, 319–330, [https://doi.org/10.1007/978-1-4020-](https://doi.org/10.1007/978-1-4020-6772-3_24)
443 [6772-3_24](https://doi.org/10.1007/978-1-4020-6772-3_24), 2008.
- 444 Bachman, S. D., Fox-Kemper, B., Taylor, J. R., and Thomas, L. N.: Parameterization of frontal symmetric instabilities. I:
445 Theory for resolved fronts, Ocean Model., 109, 72–95, <https://doi.org/10.1016/j.ocemod.2016.12.003>, 2017.

446 Barral, Q. B., Zakardjian, B., Dumas, F., Garreau, P., Testor, P., and Beuvier, J.: Characterization of fronts in the Western
 447 Mediterranean with a special focus on the North Balearic Front, *Prog. Oceanogr.*, 197, 102636,
 448 <https://doi.org/10.1016/j.pocean.2021.102636>, 2021.

449 Belkin, I. M., and Cornillon, P. C.: Fronts in the world ocean's Large Marine Ecosystems, In: International Council for the
 450 Exploration of the Sea, Annual Science Conference, Helsinki, Finland. CM 2007/D:21, 33 pp., 2007.

451 Bolado-Penagos, M., Sala, I., Jesús Gomiz-Pascual, J., González, C. J., Izquierdo, A., Álvarez, Ó., Vázquez, Á., Bruno, M.,
 452 and van Haren, H.: Analysis of internal soliton signals and their eastward propagation in the Alboran Sea: exploring the
 453 effect of subinertial forcing and fortnightly variability, *Prog. Oceanogr.*, 217, 103077,
 454 <https://doi.org/10.1016/j.pocean.2023.103077>, 2023.

455 Bonaduce, A., Cipollone, A., Johannessen, J. A., Staneva, J., Raj, R. P., and Aydogdu, A.: Ocean mesoscale variability: a case
 456 study on the Mediterranean sea from a re-analysis perspective, *Front. Earth Sci.*, 9, 816,
 457 <https://doi.org/10.3389/feart.2021.724879>, 2021.

458 Brett, G. J., Pratt, L. J., Rypina, I. I., and Sánchez-Garrido, J. C.: The western Alboran gyre: An analysis of its properties and
 459 its exchange with surrounding water, *J. Phys. Oceanogr.*, 50, 3379–3402, <https://doi.org/10.1175/JPO-D-20-0028.1>, 2020.

460 Canuto, V. M., Cheng, Y., and Howard, A. M.: Vertical diffusivities of active and passive tracers, *Ocean Model.*, 36, 198–
 461 207, <https://doi.org/10.1016/J.OCEMOD.2010.12.002>, 2011.

462 Capó, E. and McWilliams, J. C.: Coherent lagrangian pathways near an east Alboran front, *J. Geophys. Res. Ocean.*, 127,
 463 e2021JC018022, <https://doi.org/10.1029/2021JC018022>, 2022.

464 Capó, E., Orfila, A., Mason, E., and Ruiz, S.: Energy conversion routes in the western Mediterranean sea estimated from eddy-
 465 mean flow interactions, *J. Phys. Oceanogr.*, 49, 247–267, <https://doi.org/10.1175/JPO-D-18-0036.1>, 2019.

466 Carpenter, J. R., Rodrigues, A., Schultze, L. K. P., Merckelbach, L. M., Suzuki, N., Baschek, B., and Umlauf, L.: Shear
 467 Instability and Turbulence Within a Submesoscale Front Following a Storm, *Geophys. Res. Lett.*, 47, e2020GL090365,
 468 <https://doi.org/10.1029/2020GL090365>, 2020.

469 Chapman, C. C., Lea, M. A., Meyer, A., Sallée, J. B., and Hindell, M.: Defining Southern Ocean fronts and their influence on
 470 biological and physical processes in a changing climate, <https://doi.org/10.1038/s41558-020-0705-4>, 24 February 2020.

471 Chen, S., Wells, M. L., Huang, R. X., Xue, H., Xi, J., and Chai, F.: Episodic subduction patches in the western North Pacific
 472 identified from BGC-Argo float data, *Biogeosciences*, 18, 5539–5554, <https://doi.org/10.5194/bg-18-5539-2021>, 2021.

473 Crowe, M. N., and Taylor, J. R.: The evolution of a front in turbulent thermal wind balance. Part 1. Theory, *J. Fluid Mech.*,
 474 850, 179–211, <https://doi.org/10.1017/jfm.2018.448>, 2018.

475 Cushman-Roisin, B. and Beckers, J.-M.: Introduction to Geophysical Fluid Dynamics: Physical and Numerical Aspects,
 476 Academic Press, ISBN: 978-0-12-088759-0, 2011.

477 Cutolo, E., Pascual, A., Ruiz, S., Shaun Johnston, T. M., Freilich, M., Mahadevan, A., Shcherbina, A., Poulain, P. M.,
 478 Ozgokmen, T., Centurioni, L. R., Rudnick, D. L., and D'Asaro, E.: Diagnosing Frontal Dynamics From Observations

479 Using a Variational Approach, *J. Geophys. Res. Ocean.*, 127, e2021JC018336, <https://doi.org/10.1029/2021JC018336>,
480 2022.

481 Cuypers, Y., Bouruet-Aubertot, P., and Marec, C.: Characterization of turbulence from a fine-scale parameterization and
482 microstructure measurements in the Mediterranean Sea during the BOUM experiment, *Biogeosciences*, 9, 3131–3149,
483 <https://doi.org/10.5194/bg-9-3131-2012>, 2012.

484 D’asaro, E. A.: Turbulence in the upper-ocean mixed layer, *Ann. Rev. Mar. Sci.*, 6, 101–115, [https://doi.org/10.1146/annurev-](https://doi.org/10.1146/annurev-marine-010213-135138)
485 [marine-010213-135138](https://doi.org/10.1146/annurev-marine-010213-135138), 2014.

486 D’Asaro, E., Lee, C., Rainville, L., Harcourt, R., and Thomas, L.: Enhanced turbulence and energy dissipation at ocean fronts,
487 *Science*, 332, 318–322, <https://doi.org/10.1126/science.1201515>, 2011.

488 de Boyer Montégut, C., Madec, G., Fischer, A. S., Lazar, A., and Iudicone, D.: Mixed layer depth over the global ocean: An
489 examination of profile data and a profile-based climatology, *J. Geophys. Res. Ocean.*, 109, 1–20,
490 <https://doi.org/10.1029/2004JC002378>, 2004.

491 Dever, M., Freilich, M., Hodges, B., Farrar, J., Lanagan, T., and Mahadevan, A.: UCTD and ECOCTD observations from the
492 CALYPSO pilot experiment (2018): Cruise and data report. Woods Hole Oceanographic Institution Tech. Rep., WHOI-
493 2019-01, <https://doi.org/10.1575/1912/23637>, 2019.

494 Du, C., Liu, Z., Kao, S. J., and Dai, M.: Diapycnal Fluxes of Nutrients in an Oligotrophic Oceanic Regime: The South China
495 Sea, *Geophys. Res. Lett.*, 44, 11, 510–11, 518, <https://doi.org/10.1002/2017GL074921>, 2017.

496 Fedele, G., Mauri, E., Notarstefano, G., and Poulain, P. M.: Characterization of the Atlantic Water and Levantine Intermediate
497 Water in the Mediterranean Sea using 20 years of Argo data, *Ocean Sci.*, 18, 129–142, [https://doi.org/10.5194/os-18-129-](https://doi.org/10.5194/os-18-129-2022)
498 [2022](https://doi.org/10.5194/os-18-129-2022), 2022.

499 Fer, I., Dengler, M., Holtermann, P., Le Boyer, A., and Lueck, R.: ATOMIX benchmark datasets for dissipation rate
500 measurements using shear probes, *Sci. Data*, 11, 518, <https://doi.org/10.1038/s41597-024-03323-y>, 2024.

501 Fernández-Castro, B., Mouriño-Carballido, B., Benítez-Barrios, V. M., Chouciño, P., Fraile-Nuez, E., Graña, R., Piedeleu, M.,
502 and Rodríguez-Santana, A.: Microstructure turbulence and diffusivity parameterization in the tropical and subtropical
503 Atlantic, Pacific and Indian Oceans during the Malaspina 2010 expedition, *Deep. Res. Part I Oceanogr. Res. Pap.*, 94, 15–
504 30, <https://doi.org/10.1016/j.dsr.2014.08.006>, 2014.

505 Ferron, B., Bouruet-Aubertot, P., Schroeder, K., Bryden, H. L., Cuypers, Y., and Borghini, M.: Contribution of Thermohaline
506 Staircases to Deep Water Mass Modifications in the Western Mediterranean Sea From Microstructure Observations, *Front.*
507 *Mar. Sci.*, 8, 544, <https://doi.org/10.3389/fmars.2021.664509>, 2021.

508 Forryan, A., Allen, J. T., Edhouse, E., Silburn, B., Reeve, K., and Tesi, E.: Turbulent mixing in the eddy transport of Western
509 Mediterranean Intermediate Water to the Alboran Sea, *J. Geophys. Res. Ocean.*, 117, 9008,
510 <https://doi.org/10.1029/2012JC008284>, 2012.

511 Freilich, M. A., Poirier, C., Dever, M., Alou-Font, E., Allen, J., Cabornero, A., Sudek, L., Choi, C. J., Ruiz, S., Pascual, A.,
512 Farrar, J. T., Johnston, T. M. S., D’Asaro, E., Worden, A. Z., and Mahadevan, A.: 3D-intrusions transport active surface

513 microbial assemblages to the dark ocean, *bioRxiv*, 121, 2023.09.14.557835, <https://doi.org/10.1073/PNAS.2319937121>,
514 2023.

515 Freilich, M. and Mahadevan, A.: Coherent Pathways for Subduction From the Surface Mixed Layer at Ocean Fronts, *J.*
516 *Geophys. Res. Ocean.*, 126, e2020JC017042, <https://doi.org/10.1029/2020JC017042>, 2021.

517 Garcia-Jove, M., Mourre, B., Zarokanellos, N. D., Lermusiaux, P. F. J., Rudnick, D. L., and Tintoré, J.: Frontal Dynamics in
518 the Alboran Sea: 2. Processes for Vertical Velocities Development, *J. Geophys. Res. Ocean.*, 127, e2021JC017428,
519 <https://doi.org/10.1029/2021JC017428>, 2022.

520 García-Martínez, M. del C., Vargas-Yáñez, M., Moya, F., Santiago, R., Muñoz, M., Reul, A., Ramírez, T., and Balbín, R.:
521 Average nutrient and chlorophyll distributions in the western Mediterranean: RADMED project, *Oceanologia*, 61, 143–
522 169, <https://doi.org/10.1016/j.oceano.2018.08.003>, 2019.

523 Gregg, M. C.: Scaling turbulent dissipation in the thermocline, *J. Geophys. Res. Ocean.*, 94, 9686–9698,
524 <https://doi.org/10.1029/jc094ic07p09686>, 1989.

525 Gregg, M. C., D’Asaro, E. A., Riley, J. J., and Kunze, E.: Mixing efficiency in the ocean, *Ann. Rev. Mar. Sci.*, 10, 443–473,
526 <https://doi.org/10.1146/annurev-marine-121916-063643>, 2018.

527 IOC, SCOR, and IAPSO: The international thermodynamic equation of seawater – 2010: Calculation and use of
528 thermodynamic properties. Intergovernmental Oceanographic Commission, Manuals and Guides, 56, UNESCO, 196 pp.,
529 2010.

530 Johnson, A. R. and Omand, M. M.: Evolution of a Subducted Carbon-Rich Filament on the Edge of the North Atlantic Gyre,
531 *J. Geophys. Res. Ocean.*, 126, e2020JC016685, <https://doi.org/10.1029/2020JC016685>, 2021.

532 Johnston, T. M. S., Rudnick, D. L., and Pallàs-Sanz, E.: Elevated mixing at a front, *J. Geophys. Res. Ocean.*, 116, 11033,
533 <https://doi.org/10.1029/2011JC007192>, 2011.

534 Kelley, D. E., Fernando, H. J. S., Gargett, A. E., Tanny, J., and Özsoy, E.: The diffusive regime of double-diffusive convection,
535 *Prog. Oceanogr.*, 56, 461–481, [https://doi.org/10.1016/S0079-6611\(03\)00026-0](https://doi.org/10.1016/S0079-6611(03)00026-0), 2003.

536 Klein, P. and Lapeyre, G.: The oceanic vertical pump induced by mesoscale and submesoscale turbulence, *Ann. Rev. Mar.*
537 *Sci.*, 1, 351–375, <https://doi.org/10.1146/annurev.marine.010908.163704>, 2009.

538 Lazzari, P., Solidoro, C., Salon, S., and Bolzon, G.: Spatial variability of phosphate and nitrate in the Mediterranean Sea: A
539 modeling approach, *Deep. Res. Part I Oceanogr. Res. Pap.*, 108, 39–52, <https://doi.org/10.1016/j.dsr.2015.12.006>, 2016.

540 [Le Boyer, A., Couto, N., Alford, M. H., Drake, H. F., Bluteau, C. E., Hughes, K. G., Naveira Garabato, A. C., Moulin, A. J.,](#)
541 [Peacock, T., Fine, E. C., Mashayek, A., Cimoli, L., Meredith, M. P., Melet, A., Fer, I., Dengler, M., and Stevens, C. L.:](#)
542 [Turbulent diapycnal fluxes as a pilot Essential Ocean Variable, *Front. Mar. Sci.*, 10, 1241023,](#)
543 <https://doi.org/10.3389/fmars.2023.1241023>, 2023.

544 Llorc, J., Langlais, C., Matear, R., Moreau, S., Lenton, A., and Strutton, P. G.: Evaluating Southern Ocean Carbon Eddy-Pump
545 From Biogeochemical-Argo Floats, *J. Geophys. Res. Ocean.*, 123, 971–984, <https://doi.org/10.1002/2017JC012861>, 2018.

546 Lozovatsky, I. D., Fernando, H. J. S., Jinadasa, S. U. P., and Wijesekera, H. W.: Eddy diffusivity in stratified ocean: a case
547 study in Bay of Bengal, *Environ. Fluid Mech.*, 1–13, <https://doi.org/10.1007/s10652-022-09872-3>, 2022.

548 [Lueck, R., Fer, I., Bluteau, C., Dengler, M., Holtermann, P., Inoue, R., LeBoyer, A., Nicholson, S. A., Schulz, K., and Stevens,](#)
549 [C.: Best practices recommendations for estimating dissipation rates from shear probes, *Front. Mar. Sci.*, 11, 1334327,](#)
550 <https://doi.org/10.3389/fmars.2024.1334327>, 2024.

551 MacKinnon, J., St Laurent, L., and Naveira Garabato, A. C.: Diapycnal mixing processes in the ocean interior, in: *International*
552 *Geophysics*, vol. 103, Academic Press, 159–183, <https://doi.org/10.1016/B978-0-12-391851-2.00007-6>, 2013.

553 Mahadevan, A.: The Impact of Submesoscale Physics on Primary Productivity of Plankton, *Ann. Rev. Mar. Sci.*, 8, 161–184,
554 <https://doi.org/10.1146/annurev-marine-010814-015912>, 2016.

555 Mahadevan, A., Pascual, A., Rudnick, D. L., Ruiz, S., Tintoré, J., and D’Asaro, E.: Coherent pathways for vertical transport
556 from the surface ocean to interior, *Bull. Am. Meteorol. Soc.*, 101, E1996–E2004, [https://doi.org/10.1175/BAMS-D-19-](https://doi.org/10.1175/BAMS-D-19-0305.1)
557 0305.1, 2020a.

558 Mahadevan, A., D’Asaro, E. A., Allen, J. T., Almaraz García, P., Alou-Font, E., Aravind, H. M., Balaguer, P., Caballero, I.,
559 Calafat, N., Carbornero, A., Casas, B., Castilla, C., Centurioni, L. R., Conley, M., Cristofano, G., Cutolo, E., Dever, M.,
560 Enrique Navarro, A., Falcieri, F., Freilich, M., Goodwin, E., Graham, R., Guigand, C., Hodges, B. A., Huntley, H.,
561 Johnston, S., Lankhorst, M., Lermusiaux, P. F. J., Lizaran, I., Mirabito, C., Miralles, A., Mourre, B., Navarro, G., Ohmart,
562 M., Ouala, S., Ozgokmen, T. M., Pascual, A., Pou, J. M. H., Poulain, P. M., Ren, A., Rodriguez Tarry, D., Rudnick, D. L.,
563 Rubio, M., Ruiz, S., Rypina, I. I., Tintore, J., Send, U., Shcherbina, A. Y., Torner, M., Salvador-Vieira, G., Wirth, N., and
564 Zarokanellos, N.: CALYPSO 2019 Cruise Report: field campaign in the Mediterranean, Woods Hole Oceanographic
565 Institution, <https://doi.org/10.1575/1912/25266>, 2020b.

566 McDougall, T. J., Thorpe, S. A., and Gibson, C. H.: Small-Scale Turbulence and Mixing in the Ocean: A Glossary, in: *Small-*
567 *scale turbulence and mixing in the ocean*, vol. 46, edited by: Nihoul, J. C. J. and Jamart, B. M., Elsevier, 3–9,
568 [https://doi.org/10.1016/S0422-9894\(08\)70533-6](https://doi.org/10.1016/S0422-9894(08)70533-6), 1988.

569 McDougall, T. [and Krzysik, O.: Spiciness, *J. Mar. Res.*, 73, 141–152, https://doi.org/10.1357/002224015816665589, 2015](#)
570 [McDougall, T. J., Barker, P. M., and Stanley, G. J.: Spice Variables and Their Use in Physical Oceanography, *J. Geophys.*](#)
571 [Res. Ocean.](#), 126, e2019JC01593, <https://doi.org/10.1029/2019JC015936>, 2021.

572 McWilliams, J. C.: Oceanic Frontogenesis, *Ann. Rev. Mar. Sci.*, 13, 227–253, [https://doi.org/10.1146/annurev-marine-](https://doi.org/10.1146/annurev-marine-032320-120725)
573 032320-120725, 2021.

574 Mena, C., Reglero, P., Hidalgo, M., Sintés, E., Santiago, R., Martín, M., Moyà, G., and Balbín, R.: Phytoplankton community
575 structure is driven by stratification in the oligotrophic mediterranean sea, *Front. Microbiol.*, 10, 456694,
576 <https://doi.org/10.3389/fmicb.2019.01698>, 2019.

577 Mouriño-Carballido, B., Otero Ferrer, J. L., Fernández Castro, B., Marañón, E., Blazquez Maseda, M., Aguiar-González, B.,
578 Chouciño, P., Graña, R., Moreira-Coello, V., and Villamaña, M.: Magnitude of nitrate turbulent diffusion in contrasting
579 marine environments, *Sci. Rep.*, 11, 1–16, <https://doi.org/10.1038/s41598-021-97731-4>, 2021.

580 Nasmyth, P. W.: Oceanic turbulence, Ph.D. thesis, University of British Columbia, Canada,
581 <https://doi.org/10.14288/1.0302459>, 1970.

582 Oguz, T., Macias, D., Garcia-Lafuente, J., Pascual, A., and Tintore, J.: Fueling plankton production by a meandering frontal
583 jet: A case study for the Alboran sea (Western Mediterranean), *PLoS One*, 9, e111482,
584 <https://doi.org/10.1371/journal.pone.0111482>, 2014.

585 Olita, A., Capet, A., Claret, M., Mahadevan, A., Poulain, P. M., Ribotti, A., Ruiz, S., Tintoré, J., Tovar-Sánchez, A., and
586 Pascual, A.: Frontal dynamics boost primary production in the summer stratified Mediterranean sea, *Ocean Dyn.*, 67, 767–
587 782, <https://doi.org/10.1007/s10236-017-1058-z>, 2017.

588 Omand, M. M., D’Asaro, E. A., Lee, C. M., Perry, M. J., Briggs, N., Cetinić, I., and Mahadevan, A.: Eddy-driven subduction
589 exports particulate organic carbon from the spring bloom, *Science*, 348, 222–225, <https://doi.org/10.1126/science.1260062>,
590 2015.

591 Onken, R. and Brambilla, E.: Double diffusion in the Mediterranean Sea: Observation and parameterization of salt finger
592 convection, *J. Geophys. Res. Ocean.*, 108, 8124, <https://doi.org/10.1029/2002jc001349>, 2003.

593 Pinkel, R., Sherman, J., Smith, J., and Anderson, S.: Strain: Observations of the Vertical Gradient of Isopycnal Vertical
594 Displacement, *J. Phys. Oceanogr.*, 21, 527–540, [https://doi.org/10.1175/1520-0485\(1991\)021<0527:sootvg>2.0.co;2](https://doi.org/10.1175/1520-0485(1991)021<0527:sootvg>2.0.co;2),
595 1991.

596 Ramondenc, S., Madeleine, G., Lombard, F., Santinelli, C., Stemmann, L., Gorsky, G., and Guidi, L.: An initial carbon export
597 assessment in the Mediterranean Sea based on drifting sediment traps and the Underwater Vision Profiler data sets, *Deep.*
598 *Res. Part I Oceanogr. Res. Pap.*, 117, 107–119, <https://doi.org/10.1016/j.dsr.2016.08.015>, 2016.

599 Reale, M., Giorgi, F., Solidoro, C., Di Biagio, V., Di Sante, F., Mariotti, L., Farneti, R., and Sannino, G.: The Regional Earth
600 System Model RegCM-ES: Evaluation of the Mediterranean Climate and Marine Biogeochemistry, *J. Adv. Model. Earth*
601 *Syst.*, 12, e2019MS001812, <https://doi.org/10.1029/2019MS001812>, 2020.

602 Rudnick, D. L. and Klinke, J.: The underway conductivity-temperature-depth instrument, *J. Atmos. Ocean. Technol.*, 24,
603 1910–1923, <https://doi.org/10.1175/JTECH2100.1>, 2007.

604 Rudnick, D. L., Zarokanellos, N. D., and Tint, J.: A Four-Dimensional Survey of the Almeria–Oran Front by Underwater
605 Gliders: Tracers and Circulation, *J. Phys. Oceanogr.*, 52, 225–242, <https://doi.org/10.1175/JPO-D-21-0181.1>, 2022.

606 Ruiz, S., Claret, M., Pascual, A., Olita, A., Troupin, C., Capet, A., Tovar-Sánchez, A., Allen, J., Poulain, P. M., Tintoré, J.,
607 and Mahadevan, A.: Effects of Oceanic Mesoscale and Submesoscale Frontal Processes on the Vertical Transport of
608 Phytoplankton, *J. Geophys. Res. Ocean.*, 124, 5999–6014, <https://doi.org/10.1029/2019JC015034>, 2019.

609 Sala, I., Bolado-Penagos, M., Bartual, A., Bruno, M., García, C. M., López-Urrutia, Á., González-García, C., and Echevarría,
610 F.: A Lagrangian approach to the Atlantic Jet entering the Mediterranean Sea: Physical and biogeochemical
611 characterization, *J. Mar. Syst.*, 226, 103652, <https://doi.org/10.1016/j.jmarsys.2021.103652>, 2022.

612 Sánchez-Garrido, J. C. and Nadal, I.: The Alboran Sea circulation and its biological response: A review, *Front. Mar. Sci.*, 9,
613 933390, <https://doi.org/10.3389/fmars.2022.933390>, 2022.

614 Schmitt, R. W.: Double-Diffusive Convection, in: Encyclopedia of Ocean Sciences, Academic Press, 162–170,
615 <https://doi.org/10.1016/B978-012374473-9.00604-4>, 2009.

616 Schroeder, K., Chiggiato, J., Bryden, H. L., Borghini, M., and Ben Ismail, S.: Abrupt climate shift in the Western
617 Mediterranean Sea, *Sci. Rep.*, 6, 1–7, <https://doi.org/10.1038/srep23009>, 2016.

618 Schulz, K., Mohrholz, V., Fer, I., Janout, M., Hoppmann, M., Schaffer, J., and Koenig, Z.: A full year of turbulence
619 measurements from a drift campaign in the Arctic Ocean 2019–2020, *Sci. Data*, 9, 1–11, [https://doi.org/10.1038/s41597-](https://doi.org/10.1038/s41597-022-01574-1)
620 022-01574-1, 2022.

621 Sheehan, P. M. F., Damerell, G. M., Leadbitter, P. J., Heywood, K. J., and Hall, R. A.: Turbulent kinetic energy dissipation
622 rate and associated fluxes in the western tropical Atlantic estimated from ocean glider observations, *Ocean Sci.*, 19, 77–
623 92, <https://doi.org/10.5194/os-19-77-2023>, 2023.

624 Shroyer, E. L., Nash, J. D., Waterhouse, A. F., and Moum, J. N.: Measuring Ocean Turbulence, in: *Observing the Oceans in*
625 *Real Time*, edited by: Venkatesan, R., Tandon, A., D’Asaro, E., and Atmanand, M. A., Springer, Cham, 99–122,
626 https://doi.org/10.1007/978-3-319-66493-4_6, 2018.

627 Storer, B. A., Buzzicotti, M., Khatri, H., Griffies, S. M., and Aluie, H.: Global energy spectrum of the general oceanic
628 circulation, *Nat. Commun.*, 13, 1–9, <https://doi.org/10.1038/s41467-022-33031-3>, 2022.

629 Stukel, M. R., Aluwihare, L. I., Barbeau, K. A., Chekalyuk, A. M., Goericke, R., Miller, A. J., Ohman, M. D., Ruacho, A.,
630 Song, H., Stephens, B. M., and Landry, M. R.: Mesoscale ocean fronts enhance carbon export due to gravitational sinking
631 and subduction, *Proc. Natl. Acad. Sci. U. S. A.*, 114, 1252–1257, <https://doi.org/10.1073/pnas.1609435114>, 2017.

632 Sudre, F., Hernández-Carrasco, I., Mazoyer, C., Sudre, J., Dewitte, B., Garçon, V., and Rossi, V.: An ocean front dataset for
633 the Mediterranean sea and southwest Indian ocean, *Sci. Data*, 10, 1–15, <https://doi.org/10.1038/s41597-023-02615-z>, 2023.

634 Tanhua, T., Hainbucher, D., Schroeder, K., Cardin, V., Álvarez, M., and Civitarese, G.: The Mediterranean Sea system: A
635 review and an introduction to the special issue, *Ocean Sci.*, 9, 789–803, <https://doi.org/10.5194/os-9-789-2013>, 2013.

636 Taylor, G. I.: Statistical theory of turbulence, *Proc. R. Soc. London. Ser. A - Math. Phys. Sci.*, 151, 421–444,
637 <https://doi.org/10.1098/rspa.1935.0158>, 1935.

638 Thomas, L. N., Taylor, J. R., Ferrari, R., and Joyce, T. M.: Symmetric instability in the Gulf Stream, *Deep. Res. Part II Top.*
639 *Stud. Oceanogr.*, 91, 96–110, <https://doi.org/10.1016/j.dsr2.2013.02.025>, 2013.

640 Thorpe, S. A.: An introduction to ocean turbulence, Cambridge University Press, England, 291 pp.,
641 <https://doi.org/10.1017/CBO9780511801198>, 2007.

642 Thorpe, S. A.: The turbulent ocean, Cambridge University Press, England, 439 pp.,
643 <https://doi.org/10.1017/CBO9780511819933>, 2005.

644 van der Boog, C. G., Dijkstra, H. A., Pietrzak, J. D., and Katsman, C. A.: Double-diffusive mixing makes a small contribution
645 to the global ocean circulation, *Commun. Earth Environ.*, 2, 1–9, <https://doi.org/10.1038/s43247-021-00113-x>, 2021.

646 van Haren, H.: Sensitive Temperature Probes Detail Different Turbulence Processes in the Deep Mediterranean,
647 *Oceanography*, 36, <https://doi.org/10.5670/OCEANOGRAPHY.2023.108>, 2023.

648 van Haren, H., Millot, C., and Taupier-Letage, I.: Fast deep sinking in Mediterranean eddies, *Geophys. Res. Lett.*, 33, 4606,
649 <https://doi.org/10.1029/2005GL025367>, 2006.

650 Vladioiu, A., Bouruet-Aubertot, P., Cuypers, Y., Ferron, B., Schroeder, K., Borghini, M., and Leizour, S.: Contrasted mixing
651 efficiency in energetic versus quiescent regions: Insights from microstructure measurements in the Western Mediterranean
652 Sea, *Prog. Oceanogr.*, 195, 102594, <https://doi.org/10.1016/j.pocean.2021.102594>, 2021.

653 Williams, C., Sharples, J., Green, M., Mahaffey, C., and Rippeth, T.: The maintenance of the subsurface chlorophyll maximum
654 in the stratified western Irish Sea, *Limnol. Oceanogr. Fluids Environ.*, 3, 61–73, [https://doi.org/10.1215/21573689-](https://doi.org/10.1215/21573689-2285100)
655 2285100, 2013.

656 Williams, R. G.: Ocean Subduction, in: *Encyclopedia of Ocean Sciences: Second Edition*, Academic Press, 156–166,
657 <https://doi.org/10.1016/B978-012374473-9.00109-0>, 2001.

658 Yebra, L., Herrera, I., Mercado, J. M., Cortés, D., Gómez-Jakobsen, F., Alonso, A., Sánchez, A., Salles, S., and Valcárcel-
659 Pérez, N.: Zooplankton production and carbon export flux in the western Alboran Sea gyre (SW Mediterranean), *Prog.*
660 *Oceanogr.*, 167, 64–77, <https://doi.org/10.1016/j.pocean.2018.07.009>, 2018.

661 Zarokanellos, N. D., Rudnick, D. L., Garcia-Jove, M., Mourre, B., Ruiz, S., Pascual, A., and Tintoré, J.: Frontal Dynamics in
662 the Alboran Sea: 1. Coherent 3D Pathways at the Almeria-Oran Front Using Underwater Glider Observations, *J. Geophys.*
663 *Res. Ocean.*, 127, e2021JC017405, <https://doi.org/10.1029/2021JC017405>, 2022.

664 Zhmur, V. V., Novoselova, E. V., and Belonenko, T. V.: Potential Vorticity in the Ocean: Ertel and Rossby Approaches with
665 Estimates for the Lofoten Vortex, *Izv. - Atmos. Ocean Phys.*, 57, 632–641, <https://doi.org/10.1134/S0001433821050157>,
666 2021.

667 Zhou, H., Dewar, W., Yang, W., Liu, H., Chen, X., Li, R., Liu, C., and Gopalakrishnan, G.: Observations and modeling of
668 symmetric instability in the ocean interior in the Northwestern Equatorial Pacific, *Commun. Earth Environ.*, 3, 1–11,
669 <https://doi.org/10.1038/s43247-022-00362-4>, 2022.

670 Zippel, S. F., Farrar, J. T., Zappa, C. J., and Plueddemann, A. J.: Parsing the Kinetic Energy Budget of the Ocean Surface
671 Mixed Layer, <https://doi.org/10.1029/2021GL095920>, 28 January 2022.

672